Analysis and Design of an Axial Flux Permanent Magnet Motor for in-Wheel System Using a Novel Analytical Method Combined With a Numerical Method

BYUNG-OH TAK AND JONGSUK RO, (Member, IEEE)

Department of Electronic and Electrical Engineering, Chung-Ang University, Seoul 06974, South Korea

Corresponding author: Jongsuk Ro (jongsukro@gmail.com)

ABSTRACT Recently, a motor for an in-wheel system—which is advantageous when applied to electric vehicles and self-driving systems—has received much attention. In this paper, we propose an analysis and design method that can be used for an in-wheel motor. In-wheel motors require high torque density and a compact form factor to be wheel-mounted. To meet these requirements, an axial flux permanent magnet motor is proposed for the in-wheel system. The end-winding length of the coil is a key factor to be considered in this design. Hence, we propose a novel method to study the end-winding length. Due to the structural characteristics of an axial flux permanent magnet motor, a three-dimensional finite element analysis, which requires much time and expense, is essential. To solve this problem, we propose a novel analytical method combined with finite element analysis to mitigate the time and cost factors in the development of the axial flux permanent magnet motor. The magnetic saturation and the slot opening effect, which are considered during the analysis and design phase, are extremely difficult to analyze due to their nonlinearity. Therefore, a novel analytical method and algorithm, which can consider nonlinear effects, such as the magnetic saturation and slot opening, is proposed. The usefulness of the proposed analysis and design method and the axial flux permanent magnet motor for an in-wheel system were verified via 3D finite element analysis using a commercial simulation tool (JMAG).

INDEX TERMS Axial flux permanent magnet motor, electric vehicle analytical method, flux concentration, in-wheel system, magnetic equivalent circuit, magnetic saturation, quasi-3D, slot opening effect.

I. INTRODUCTION

In recent years, the electric vehicle market has been rapidly growing in keeping up with global trends—as advanced countries adopt eco-friendly policies due to climate change, environmental pollution, and the depletion of fossil fuels [1], [2]. In addition, as the self-driving vehicle market has grown, so too has the convergence of automobiles and information and communication technologies (ICT). Consequently, motors for an in-wheel system, which has advantages in applications alongside emerging autonomous driving

technologies, such as electronic stability control and smart parking assist systems, is receiving great attention.

An in-wheel system is a system that drives the wheels using wheel-mounted drive motors and control motors. Because individual control of each wheel is possible, it is relatively simple to apply ICT. However, the available space for an electric motor in an in-wheel system is limited by the wheel size because the motor is installed inside the wheel itself. Consequently, the electric motor must be compact and have a high torque density within the constraints of these dimensions [3]–[5]. In this paper, considering these constraints, a flow chart of the design and analysis process of the motor for an in-wheel system is proposed in three stages: fundamental

The associate editor coordinating the review of this manuscript and approving it for publication was Shihong Ding.

design of the motor, no-load magnetic field analysis of the motor using the proposed analytical method, and finite element analysis (FEA) of the designed motor.

An axial flux permanent magnet (AFPM) motor for an electric vehicle's in-wheel system can be designed following the process proposed in this paper. AFPM motors boast higher power density, torque density, and efficiency, compared to radial magnetic flux type permanent magnet motors of the same volume and weight, and are advantageous for miniaturization and disk shape manufacturing because they exhibit no change in performance based on shaft length [6]–[8].

Research on all motors including AFPM motors can be largely categorized into analysis and design, materials, and control. Analysis and design research mainly focuses on multiphysics modeling, such as electromagnetic field, stress, vibration, noise, and heat, design through these analyses, and analytical methods to reduce the analysis time and cost of the motors [9]–[11]. Materials research is actively conducted for the purpose of improving performance or reducing manufacturing costs by using materials such as amorphous cores and ferrite magnets [12]–[14]. Control research focuses on the development of inverters and sensors for speed and stability control of motors, motor fault detection and diagnosis, and fault tolerance control [15]–[18]. In this study, considering these various motor research issues, a novel analytical method is studied in which numerical methods are combined to reduce the time and cost required for motor design and electromagnetic field analysis.

In general, when designing a motor, its design parameters are determined using sizing equations [19]–[23]. One issue to be aware of is that a gap occurs due to the end-winding in the segment where the coil is wound around the stator, and this affects the total diameter of the motor. A method to find the end-winding length was proposed in [24]. However, it is actually determined by the minimum bend radius of copper, the material of the coil. In this paper, a novel equation that more accurately calculates the end-winding length by applying the minimum bend radius to the bending of the coil occurring at the corner of each core is first proposed.

FEA is generally used for electric machine characteristic analysis [25]–[28]. FEA is a time consuming but highly accurate analysis method. FEA does not take more than one hour when the analysis target is a two-dimensional (2D) model, but in the case of a three-dimensional (3D) model, it can take a day or more to complete. The AFPM machine requires a very long analysis time because a 3D model analysis is required due to its structural characteristics, which leads to an increase in design time and cost.

In this paper, an analytical method is proposed to solve this problem, which significantly lowers the analysis time by creating an analytical model that combines the quasi-3D method and a magnetic equivalent circuit (MEC). As shown in Fig. 1, the quasi-3D method is used to approximate the 3D analysis results by uniformly dividing the AFPM machine into multiple 2D cross-sectional models and combining the analysis
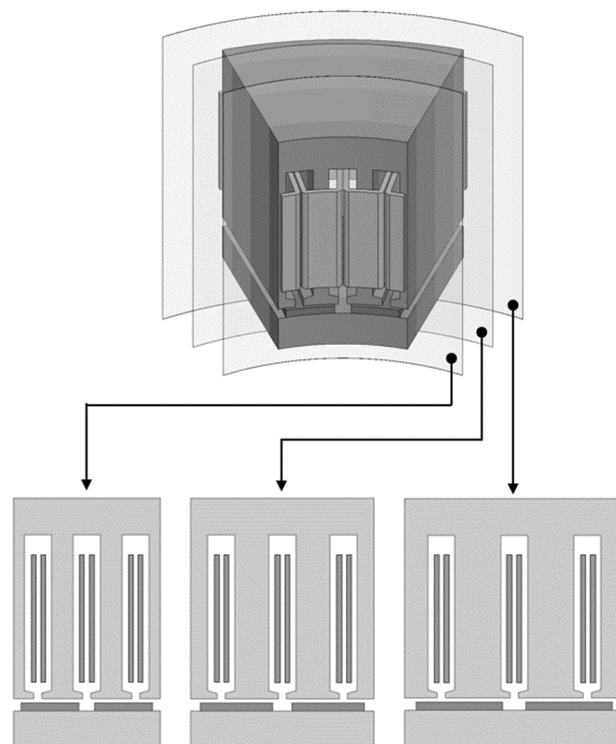

FIGURE 1. The principle of the quasi-3D method.

results [29]–[31]. The MEC method is used to analyze the characteristics of the model by simplifying the structure of the motor to be designed into a magnetic circuit form. The MEC modeling used in this study was proposed in [32]–[36]. However, in [32]–[36], the MEC modeling was conducted under the assumption that magnetic saturation did not occur. Because the magnetic saturation of the AFPM motor mainly occurs in the stator, this paper proposes a novel MEC that adds a stator core reluctance to address this.

If the cross-sectional area of the iron core through which the magnetic flux passes is insufficient compared to the magnetic field strength of the permanent magnet, the magnetic saturation effect may occur. In the case of a motor, the magnetic saturation effect is likely to occur in the stator core, and it is a factor that can significantly reduce the performance of the machine, so it must be considered [37]. To consider this, various methods for inducing the relative permeability of the iron core by approximation and interpolation of the *B-H* relationship, based on the *B-H* curve characteristic data of the iron core material, have been proposed [38]–[43]. In this paper, a method to calculate the relative permeability function using a piecewise cubic Hermite interpolating polynomial (PCHIP), based on the *B-H* curve data, is proposed, as is a novel stator core permeability correction algorithm applicable to the proposed MEC.

The slot opening effect is a phenomenon occurring in the slot opening of a machine, and it is a matter to be considered when designing a motor because it distorts the waveform of

the air-gap magnetic flux density and changes the electromagnetic characteristics of the machine [44]–[47]. In this paper, two methods are used to consider the slot opening effect. The first method is to use a conformal transformation based on complex functions. This method for an AFPM machine was proposed in [48]. However, in [48], there is only mention that the quasi-3D method was used, and it was not clearly formulated. Therefore, in this paper, the analysis model that considers the slot opening effect is proposed by formulating variables that change for each slice model obtained using the quasi-3D method during the process of calculating the slot opening effect through conformal transformation.

The second method is to obtain the magnetic flux concentration coefficient of the slot, which was proposed in [49]. However, [49] was a method targeting interior permanent magnet (IPM) machines. In this study, this method is first applied to an AFPM machine using the quasi-3D method, and an analysis model that considers the magnetic flux concentration effect is proposed by formulating variables that change for each slice model obtained using the quasi-3D method during the process of calculating the magnetic flux concentration coefficient.

Therefore, in this paper, a novel MEC analytical method is proposed, which applies a process for considering the slot opening effect as well as a process for considering the magnetic saturation of the stator. The proposed method has much faster analysis speed than FEA and accuracy similar to that of FEA. The accuracy and speed of analysis are verified by comparison with 3D FEA results.

The main reason why AFPM motors are not used extensively even though they have various advantages over conventional radial flux permanent magnet (RFPM) motors is that, as mentioned earlier, the design and analysis of AFPM motors are time-consuming and expensive owing to their structural characteristics. Therefore, the main objective of this study is to significantly reduce the time required for designing AFPM motors through the proposed analytical method.

The performance of the motor designed using the analysis and design process proposed in this paper was verified by obtaining the total harmonic distortion (THD), the back electromotive force (EMF), torque, torque ripple, power, and efficiency map through 3D FEA obtained using JMAG, a commercial tool of proven accuracy.

II. PROPOSED ANALYSIS AND DESIGN METHOD

Fig. 2(a) outlines the design and analysis process of the proposed electric vehicle in-wheel motor. This process comprises Stages A, B, and C, and Fig. 2(b) shows the steps of each stage in detail. This section describes the specific process involved for each step of each stage.

A. FUNDAMENTAL DESIGN OF THE MOTOR

In this stage, the initial design is preceded by selecting the motor requirements, structure, and materials, and determining the size parameters using the sizing equation.

STEP 1. DETERMINATION OF DESIGN TARGET AND REQUIREMENTS

This study is aimed at the in-wheel motors of electric vehicles, so the required performance is determined by accounting for this. For example, the required performance of a car can be represented using a simple dynamic model [23]. For a car to move, it must have a driving force greater than the minimum driving force of the vehicle. The minimum driving force F_{rm} can be expressed as the sum of the rolling resistance force f_{ro}, the climbing resistance force f_{st}, and the aerodynamic drag force f_l:

$$F_{rm} = f_{ro} + f_{st} + f_l \qquad (1)$$

The rolling resistance force is determined by the tire conditions on the road, as follows:

$$f_{ro} = f_r \cdot M \cdot g \qquad (2)$$

where f_r, M, and g are the rolling resistance coefficient, the vehicle mass, and the gravitational acceleration, respectively. The climbing resistance force is determined by:

$$f_{st} = M \cdot g \cdot \sin \delta \qquad (3)$$

where δ is the angle between the vehicle on horizontal ground and the slope. Since air is a Newtonian fluid, Newton's law of viscosity applies. So, the aerodynamic drag force is determined by:

$$f_l = \frac{1}{2} \rho_a \cdot C_d \cdot A_p \cdot (v + v_0)^2 \qquad (4)$$

where ρ_a is the air density, C_d is the air-resistance coefficient, A_p is the frontal projected area, v is the vehicle speed, v_0 is the headwind speed.

Therefore, the minimum torque for the vehicle to travel on a slope of angle δ is:

$$\tau_{\min} = r \times F_{rm} \qquad (5)$$

where r is the position vector. The minimum power required is:

$$P_{\min} = \tau_{\min} \cdot \omega_m \qquad (6)$$

where ω_m is the angular speed. For the vehicle to accelerate, additional power is required, depending on the required acceleration. The force applied when the vehicle accelerates is called the acceleration resistance force. It is also called the inertia resistance force, as it is a force that overcomes the inertia of the vehicle and can be expressed as:

$$f_a = (M + \Delta M) \cdot \frac{a}{g} \qquad (7)$$

where ΔM is the equivalent mass of rotating parts and changes according to the transmission ratio of the vehicle, and a is the required acceleration.

Therefore, the additional torque and power required for the vehicle to accelerate is:

$$\tau_a = r \times f_a \qquad (8)$$

$$P_a = \tau_a \cdot \omega_m \qquad (9)$$

(a)

A. Fundamental design of the motor

Start

Step 1.
Determination of design target and requirements

Step 2.
Selection of motor topology

Step 3 to 5.
Determination of the motor components and parameters

B. No-load magnetic field analysis of the motor using proposed analytical method

Step 6.
No-load magnetic field analysis using proposed analytical method

Step 7.
Consideration of magnetic saturation in the proposed analytical method

Update and recalculate with the core permeability

Check the suitability of the core permeability — No
Yes

Step 8 to 9.
Consideration of slot opening effect in the proposed analytical method

Check the suitability of the air-gap magnetic flux density — No
Yes

C. FEA of the designed motor

Step 10.
Applying cogging torque reduction technique

Step 11.
FEA of electromagnetic characteristics of the designed motor

Satisfying the required performance — No
Yes

Step 12.
confirming the final parameters of the designed motor

End

(b)

A. Fundamental design of the motor

Start

Step 1.
Determination of design target and requirements

Step 2.
Selection of motor topology

Step 3.
Selection of pole-slot number

Step 4.
Determination of the core and permanent magnet material

Step 5.1.
Determination of the main dimensions

Step 5.2.
Determination of the total diameter using end-winding length equation

B. No-load magnetic field analysis of the motor using proposed analytical method

Stator core permeability correction algorithm of the motor

$n = 1$

Step 6.1.
MEC modeling of slotless motor

Step 6.2.
Calculation of the reluctances of the propoesd MEC

Step 6.3.
Calculation of air-gap flux density of proposed MEC

Step 6.4.
Applying proposed quasi-3D method to MEC

Recalculation of stator core reluctance

Step 7.1.
Interpolation of stator core permeability function

Step 7.2.
Calculation of stator core permeability of slotless motor

$\mu_{rs,new}(B) = \mu_{rs,n}(B_{s,slotless})$

$n = n+1$

$\mu_{rs,n}(B_{s,slotless}) = \mu_{rs,n+1}(B_{s,slotless})$ — No
Yes

$\mu_{rs,n}(B_{s,slotless}) = \mu_{rs}(B_{s,slotless})$

Step 8.1.
Determination of slot opening effect coefficient

Step 8.2.
Applying quasi-3D method to slot opening effect coefficient

Step 8.3.
Determination of flux concentration coefficient

Step 8.4.
Applying quasi-3D method to flux concentration coefficient

Step 9.
Calculation of magnetic flux density of the slotted motor

$B_{s,slotted} \leq B_{s,max}$ — No
Yes

$B_{g,slotted} = B_{designed}$ — No
Yes

C. FEA of the designed motor

Step 10.
Applying cogging torque reduction technique

Step 11.1.
No-load analysis using FEA

Step 11.2.
Load analysis using FEA

Satisfying the required performance — No
Yes

Step 12.
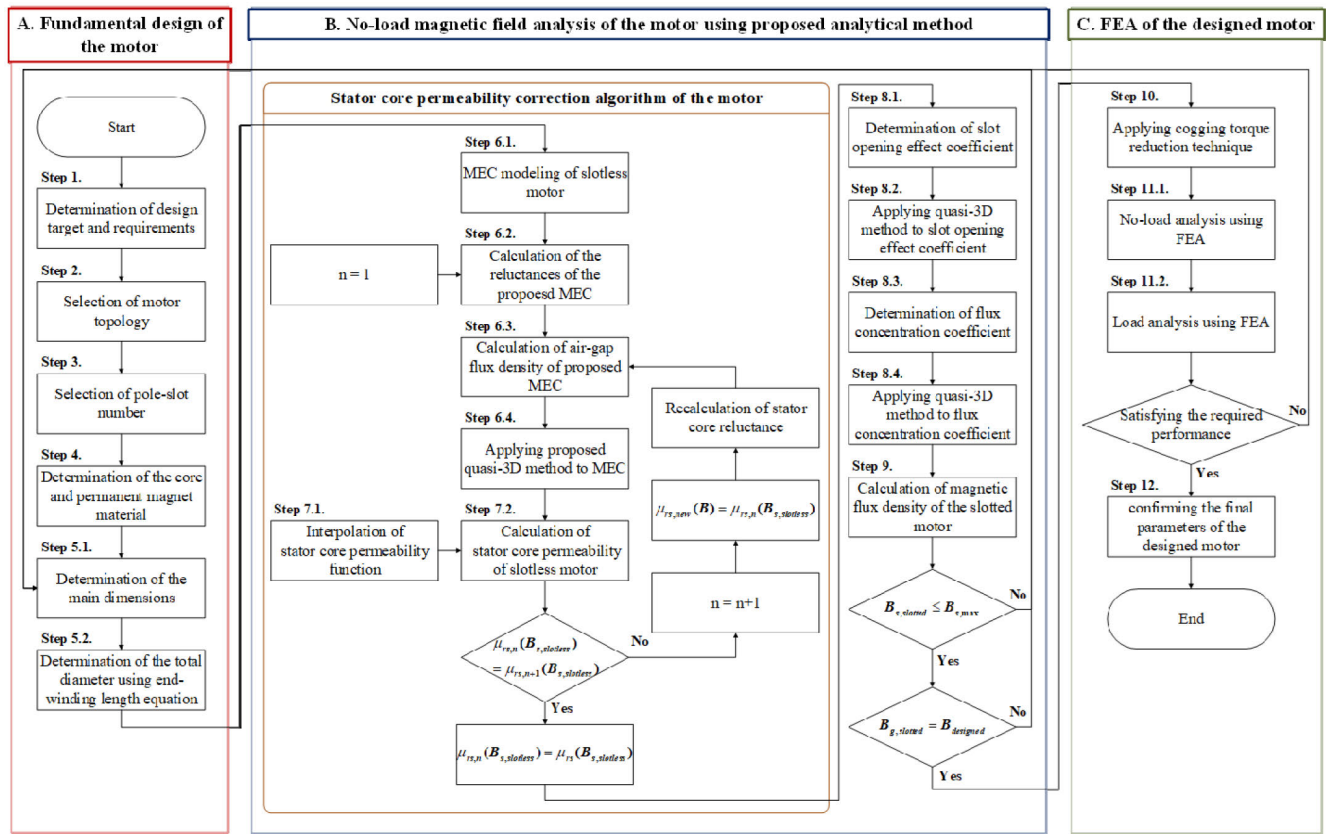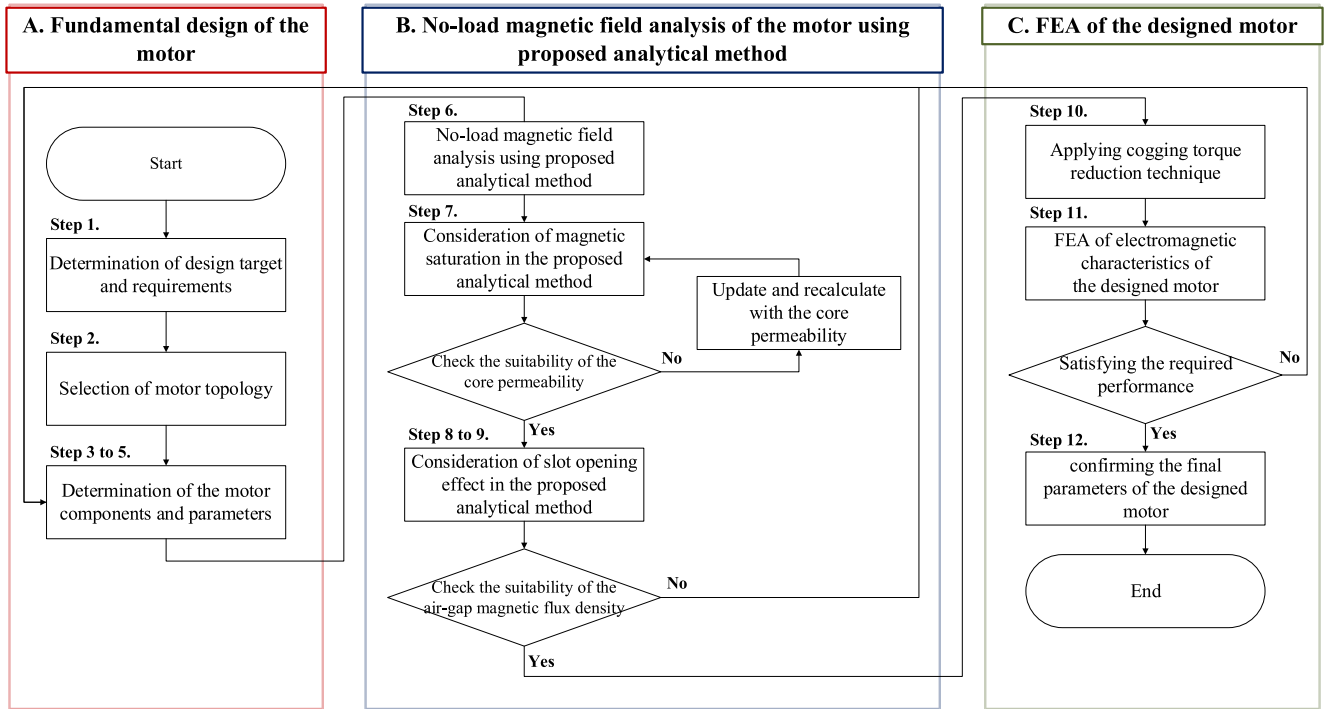confirming the final parameters of the designed motor

End

FIGURE 2. Design and analysis flow chart diagram of the motor for an electric vehicle in-wheel system (a) simplified version (b) detail version.

The total power required is:

$$P_{out} = P_a + P_{min} \qquad (10)$$

The required performance of the vehicle can be determined through (1) to (10).

STEP 2. SELECTION OF MOTOR TOPOLOGY

The size of the motor is a key requirement as the electric vehicle in-wheel motor must be mounted inside the vehicle wheel. In particular, the axial length must be short, and despite the limited size, sufficient power and torque to drive the vehicle are required. In this paper, an AFPM motor was selected to meet these requirements. Unlike conventional motor structures, the AFPM motor can effectively generate torque in a confined space—with a thin structure and a large diameter—because the main magnetic flux flows in the axial direction [50], [51]. Therefore, it is suitable for use as an in-wheel motor, as proposed in this paper.

The AFPM motor can be designed in various topologies, as shown in Fig. 3, depending on the configuration of the stator and rotor, and the arrangement of the permanent magnets [52]. In this paper, a single-stator & dual-rotor structure was adopted to increase the amount of torque generated. This structure can be of two types depending on the permanent magnet arrangement of the two rotors: north-north (NN) and north-south (NS) topologies. In the NN topology, performance loss due to magnetic saturation may occur if the thickness of the stator yoke is not large enough. However, since the NS topology has a structure in which the magnetic flux of the one rotor flows to the opposite rotor, rather than the stator yoke, the design is simplified. Therefore, the design incorporated the NS type topology. In addition, to maximize the advantage of the magnetic flux not flowing to the stator yoke, the design was carried out with a yokeless and segmented armature (YASA) topology, with the stator yoke removed. The YASA structure is easy to manufacture, can reduce the stator iron loss, and since it is made of a split core, it has the advantage of high-efficiency operation and high power density, as it can improve the coil area and reduce copper loss [53]–[55]. Therefore, in this paper, we used the YASA AFPM topology for the in-wheel system.

STEP 3. SELECTION OF POLE-SLOT NUMBER

In this step, the combination of the number of poles and slots of the motor is selected. Since the magnetic flux distribution in the stator becomes more uniform as the number of poles increases, the saturation in the core decreases even when the same current is applied. Therefore, the magnetic flux linkage by the permanent magnet does not decrease in a precisely inversely proportional manner, as the number of poles increases. In other words, the torque of the motor increases, as the number of poles increases [56]. Therefore, a multi-pole structure was adopted to design a high torque motor. However, for stable performance control, the switching frequency of the inverter must be ten times (or more) that of the electrical

frequency at the maximum speed of the motor [56]. Consequently, considering this, the number of poles of the motor designed in this paper was set to 20. The fundamental winding factor, winding layout, periodicity, and cogging multiplier were considered to determine the appropriate number of slots for the number of poles [47], [48]. In addition, the design of fractional slots, such as a combination of 2-poles–3-slots or 3-poles–4-slots, uses the asymmetry of the magnetic circuit to cancel spatial harmonics, thereby reducing the back EMF harmonics and torque ripple. Consequently, considering all these factors, a 20-poles–30-slots structure was selected.

STEP 4. DETERMINATION OF THE CORE AND PERMANENT MAGNET MATERIAL

When designing a motor, the material of the core and the permanent magnet should be determined by comprehensively considering the performance, cost, and commercialization of the motor. In this paper, 35JN230 electric steel plate and N36Z permanent magnet material were selected for the AFPM motor in-wheel system requirements.

STEP 5. DETERMINATION OF THE PARAMETERS USING SIZING EQUATIONS

Various size parameters of the motor can be determined using sizing equations. Here, the size parameter is determined using the sizing equation proposed in [19] and proposing a novel equation to consider the end-winding length.

5.1. DETERMINATION OF MAIN DIMENSIONS

In general, when the leakage resistance and inductance of the stator are neglected, the main dimensions of the electrical machine can be obtained through the output power equation for electrical machines, expressed as:

$$P_{out} = \eta \frac{m}{T} \int_0^T e(t)\, i(t)dt = mK_p \eta E_{pk} I_{pk} \qquad (11)$$

where E_{pk} is the peak value of the phase air-gap EMF, I_{pk} is the peak value of the phase current, η is the machine efficiency, m is the number of machine phases, and T is the period of one EMF cycle. K_p is the electrical power waveform factor, defined as:

$$K_p = \frac{1}{T} \int_0^T \frac{e(t) \cdot i(t)}{E_{pk} \cdot I_{pk}} dt = \frac{1}{T} \int_0^T f_e(t) \cdot f_i(t)dt \qquad (12)$$

where $f_e(t) = e(t)/E_{pk}$ and $f_i(t) = i(t)/I_{pk}$ are expressions for the normalized EMF and current waveforms.

The EMF of AFPM machine $e(t)$ is:

$$e(t) = d\frac{\Lambda_g}{dt} = K_e N_t B_g \frac{f}{p}(1 - \lambda_D^2)D_{out}^2 f_e(t) \qquad (13)$$

where Λ_g is the air-gap linkage flux per phase, p is the machine pole pair, K_e is the EMF factor which incorporates the winding distribution factor K_w and the ratio between the area spanned by the (salient) poles and the total air-gap area, N_t is the number of winding turns per phase, and γ is the
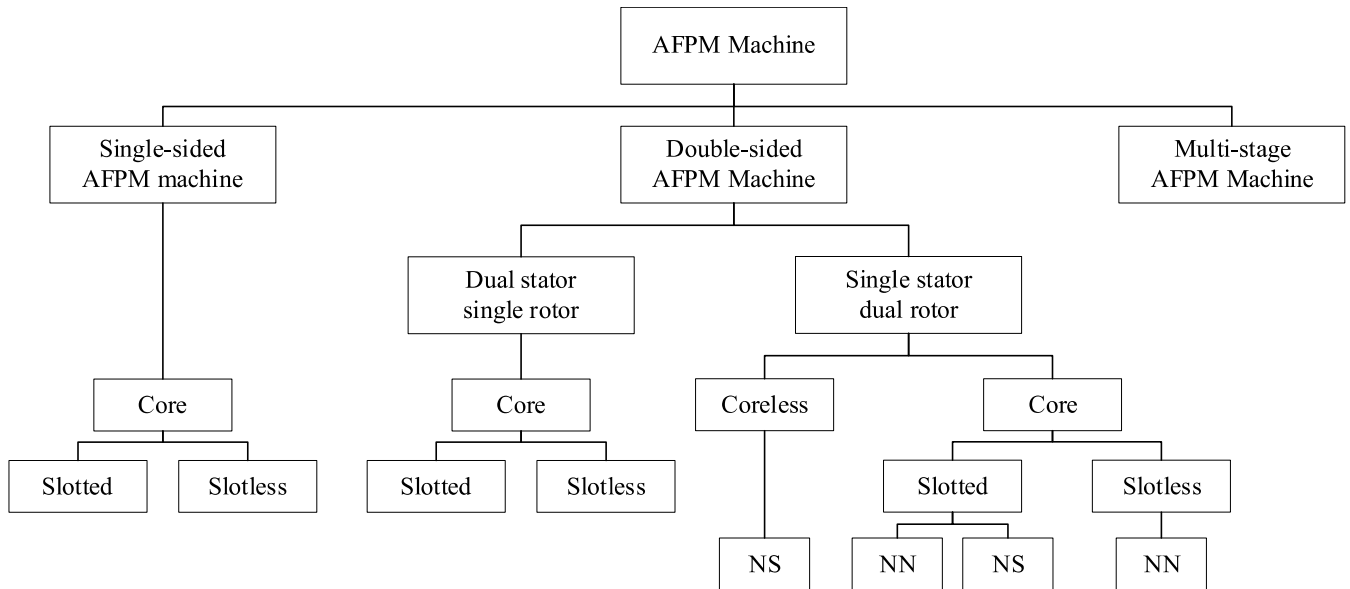
FIGURE 3. Topologies of the AFPM machine.

diameter ratio of the AFPM machine defined as:

$$\lambda_D = \frac{D_{in}}{D_{out}} \qquad (14)$$

where D_{out} is the outer diameter of the AFPM machine, and D_{in} is the inner diameter of the AFPM machine.

Through (13), E_{pk} can be obtained as:

$$E_{pk} = K_e N_t B_g \frac{f}{p}(1 - \lambda_D^2)D_{out}^2 \qquad (15)$$

For the effect of the current, the current waveform factor K_i is defined as:

$$K_i = \frac{I_{pk}}{I_{rms}} = \left(\frac{1}{T}\int_0^T \left(\frac{i(t)}{I_{pk}}\right)^2 dt\right)^{-\frac{1}{2}} \qquad (16)$$

where I_{rms} is the *rms* value of the phase current.

Table I lists typical waveforms and their corresponding power waveform factor K_p and current waveform factor K_i. I_{pk} is determined as:

$$I_{pk} = A\pi K_i \frac{1 + \lambda_D}{2}\frac{D_{out}}{2m_1 N_{ph}} \qquad (17)$$

where m_1 is the number of phases of each stator, and A is the electrical loading. Substituting (15) and (17) for (11), P_{out} is:

$$P_{out} = \frac{1}{1 + k_\phi}\frac{m}{m_1}\frac{\pi}{2}K_e K_i K_p \eta B_g A\frac{f_e}{P}(1 - \lambda_D^2)\frac{1 + \lambda_D}{2}D_{out}^3 \qquad (18)$$

To express (18) in terms of volume $D_{out}^2 L_e$, it is useful to consider the aspect ratio coefficient K_L. K_L is the coefficient related to a specific machine structure, with consideration for the effects of losses, temperature rise, and the design's efficiency requirements.

TABLE 1. Typical prototype waveforms.

Model	$e(t)$	$i(t)$	K_i	K_p
Sinusoidal			$\sqrt{2}$	$0.5\cos\phi$
Rectangular			1	1
Trapezoidal			1.134	0.777
Triangular			$\sqrt{3}$	0.333

Therefore, the sizing equation of the generally presented AFPM machine is:

$$P_{out} = \frac{1}{1 + k_\phi}\frac{m}{m_1}\frac{\pi}{2}K_e K_i K_p K_L \eta B_g A\frac{f_e}{P}(1 - \lambda_D^2)\frac{1 + \lambda_D}{2}D_{out}^2 L_e \qquad (19)$$

This equation is the key sizing equation, and it can be applied to the double-sided AFPM motor presented in this paper [59].

5.2. DETERMINATION OF TOTAL DIAMETER USING PROPOSED END-WINDING LENGTH EQUATION

In this step, the total outer diameter of the motor to be designed is obtained through the key sizing equation obtained in the previous step.
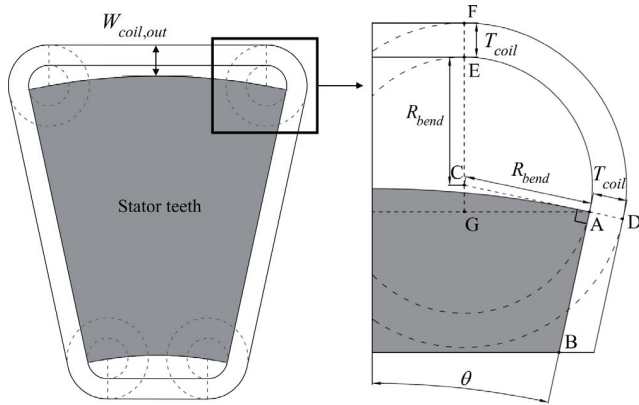
FIGURE 4. Geometry of the AFPM machine coil.

Through (18), the outer diameter D_{out} is determined as:

$$D_{out} = \sqrt[3]{\frac{P_{out}}{\frac{1}{1+k_\phi}\frac{m}{m_1}\frac{\pi}{2}K_e K_i K_p \eta B_g A \frac{f_e}{P}(1-\lambda_D^2)\frac{1+\lambda_D}{2}}} \quad (20)$$

The total outer diameter of the double-sided AFPM machine D_{out} is:

$$D_t = D_o + 2W_{coil,out} \quad (21)$$

where $W_{coil,out}$ is expressed as the sum of the thickness of the outer diameter coil and the clearance distance due to the end-winding. Since $W_{coil,out}$ is determined by the minimum bend radius of copper, the material of the coil, the equation for calculating $W_{coil,out}$ using the minimum bend radius is proposed.

Fig. 4 shows the geometry of the coil used to determine $W_{coil,out}$. θ is the outer arc angle of the stator teeth. Draw a line segment CD perpendicular to the line segment AB. The length of line segment AC is the minimum bend radius R_{bend}, and the length of AD is the thickness of the coil T_{coil}. Draw circles centered at point C, the length of segment AC and the length of AD being the radius of each circle, respectively. Through this process, the geometry of the coil can be obtained. Therefore, the end-winding length $W_{coil,out}$ is proposed as:

$$W_{coil,out} = R_{bend}(1 + \sin\theta) + N \cdot T_{coil} - \frac{D_o}{2}(1 - \cos\theta) \quad (22)$$

where N is the number of coil-wound layers.

The thickness of the coil is determined by the maximum current density, which itself is determined as $J_{max} = I_{pk}/A_{coil}$. There is a typical criterion that is dependent on the cooling method of the motor.

B. NO-LOAD MAGNETIC FIELD ANALYSIS OF THE MOTOR USING PROPOSED ANALYTICAL METHOD

It is necessary to analyze the characteristics of the machine to ensure that the motor designed in Stage A is designed
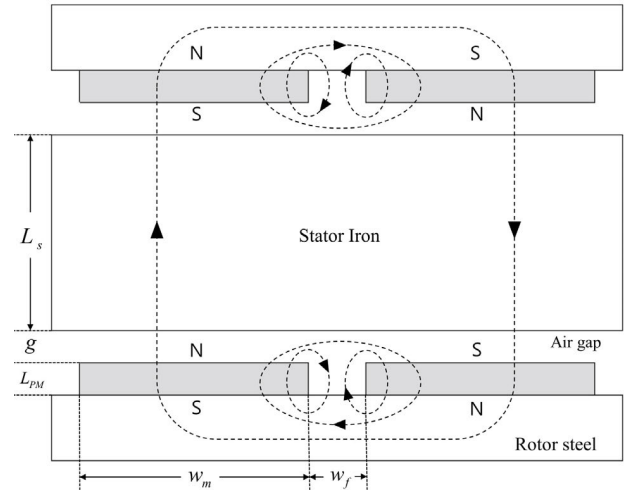
FIGURE 5. The cross-sectional structure of the AFPM motor.

correctly. FEA is used to analyze the characteristics of electric machines, and although it offers high accuracy, it consumes an enormous amount of time. Therefore, in this stage, the no-load magnetic field analytical method applicable to AFPM motors, yielding a faster analysis time compared to FEA, is proposed. In addition, to ensure that the proposed analytical method has FEA levels of accuracy, a stator core permeability correction algorithm to consider magnetic saturation and other methods that consider slot opening effects, are proposed.

STEP 6. NO-LOAD MAGNETIC FIELD ANALYSIS USING PROPOSED QUASI-3D MEC METHOD

The MEC method is used to analyze the characteristics of the model by simplifying the structure of the motor to be designed. Using this method, the average air-gap magnetic flux density of the target model can be obtained. Therefore, the MEC method for the dual-sided AFPM motor, which adds a new parameter to consider magnetic saturation using the quasi-3D method, is proposed.

STEP 6.1. MEC MODELING OF SLOTLESS MOTOR

Fig. 5 shows the cross-sectional structure of the AFPM motor cut in the radial direction [32]. To simplify the value of the parameter to be obtained using the MEC method, it is assumed that it is a slotless structure.

When designing the motor, the thickness of the rotor's back iron is designed to be sufficiently thick in consideration of the durability and magnetic saturation of the motor. Therefore, if magnetic saturation does not occur in R_r, R_r is very small compared to R_g and can be ignored. However, the stator is prone to magnetic saturation, which is directly related to the performance of the machine. Therefore, to consider performance change due to magnetic saturation, the stator core reluctance is defined. Thus, based on the three magnetic flux flows shown in Fig. 5, the MEC modeled by adding stator core reluctance is shown in Fig. 6.
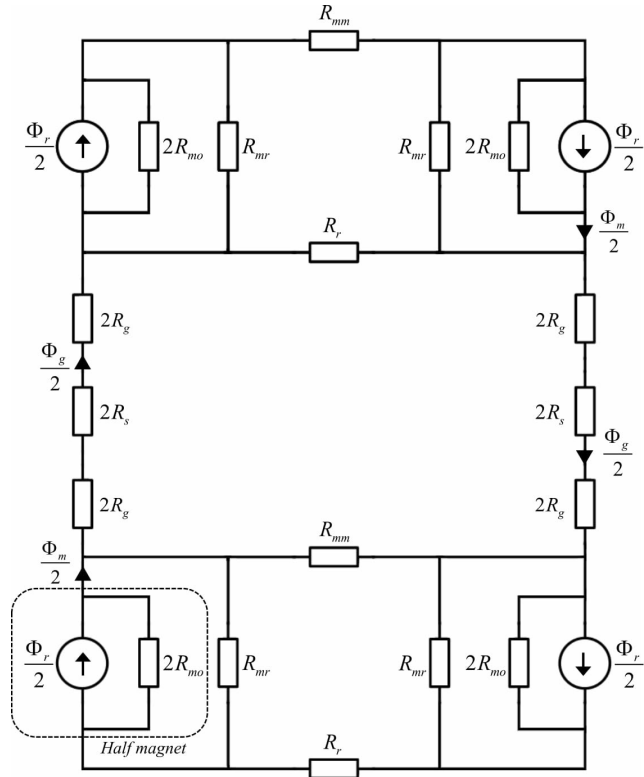
FIGURE 6. Magnetic equivalent circuit for Fig. 5.

The parameters in Fig. 6 are defined as:

Φ_g : Air-gap flux for one magnet pole

Φ_r : Flux source of one magnet pole

R_g : Reluctance of the air gap

R_{mo} : Reluctance of a magnet, corresponding to Φ_r

R_s : Reluctance of the stator

R_r : Reluctance of the rotor back iron

R_{mr} : Reluctance corresponding to the magnet-to-rotor leakage flux

R_{mm} : Reluctance corresponding to the magnet-to-magnet leakage flux

Since the circuit diagram is symmetrical, Fig. 6 can be simplified to Fig. 7 and Fig. 8.

STEP 6.2. CALCULATION OF THE RELUCTANCES OF THE PROPOSED MEC

In Fig. 6, the reluctance parameter is:

$$R_{mo} = \frac{L_{PM}}{\mu_0 \mu_{rm} A_m} \tag{23}$$

$$R_g = \frac{g}{\mu_0 A_g} \tag{24}$$

$$R_{mm} = \frac{\pi}{\mu_0 h \ln(1 + \pi g / w_f)} \tag{25}$$

$$R_{mr} = \frac{\pi}{\mu_0 h \ln \left[1 + \pi \min \left(g, \frac{w_f}{2} \right) / L_{PM} \right]} \tag{26}$$

$$R_s = \frac{L_s}{\mu_0 \mu_{rs}(B) A_g} \tag{27}$$
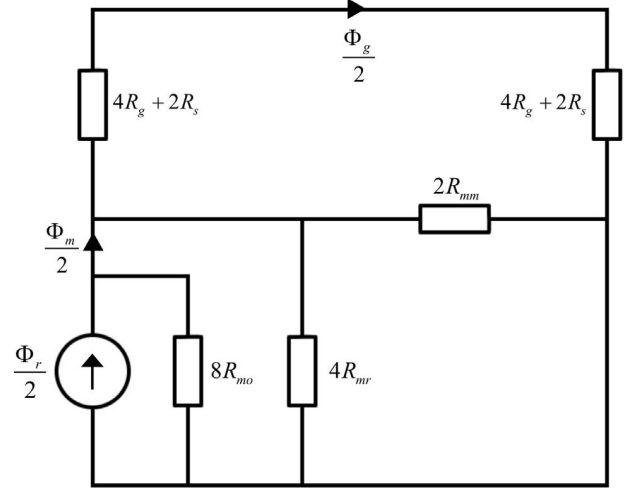
FIGURE 7. The reduced form of Fig. 6.
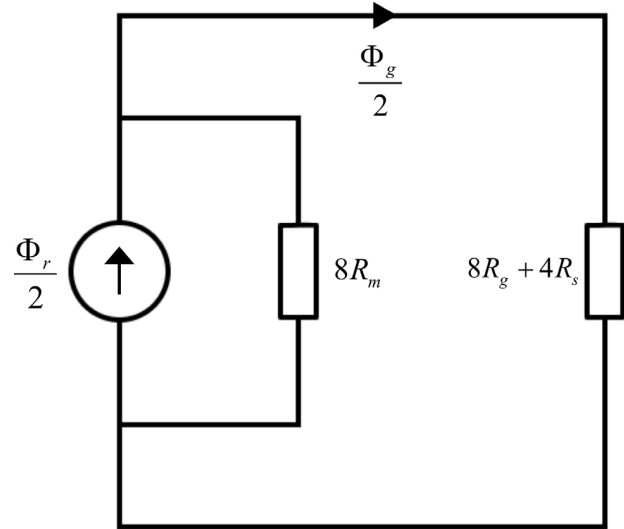
FIGURE 8. The reduced form of Fig. 7.

where:

$$A_m = w_m h \tag{28}$$

$$A_g = (w_m + 2g)h \tag{29}$$

$$h = \frac{D_{out} - D_{in}}{2} \tag{30}$$

The permeability of the stator core is $\mu_{rs}(B) = \mu_{rs,ini} = 3000$. In Fig. 8, R_m is calculated as:

$$R_m = \frac{R_{mo}}{1 + 2\alpha + 4\beta} \tag{31}$$

where:

$$\alpha = \frac{R_{mo}}{R_{mr}} \tag{32}$$

$$\beta = \frac{R_{mo}}{R_{mm}} \tag{33}$$

STEP 6.3. CALCULATION OF AIR-GAP FLUX DENSITY OF PROPOSED MEC

Using flux division, the total air-gap magnetic flux obtained by the proposed MEC method can be expressed as:

$$\Phi_g = \frac{R_m \Phi_r}{R_m + \left(R_g + \frac{R_s}{2}\right)}$$

$$= \frac{\Phi_r}{1 + \left(\frac{2R_g + R_s}{2R_{mo}}\right)(1 + 2\alpha + 4\beta)} \qquad (34)$$

$$\Phi_m = \frac{\left(R_g + \frac{R_s}{2}\right)\Phi_r}{R_m + \left(R_g + \frac{R_s}{2}\right)}$$

$$= \frac{1 + \left(\frac{2R_g + R_s}{2R_{mo}}\right)(2\alpha + 4\beta)}{1 + \left(\frac{2R_g + R_s}{2R_{mo}}\right)(1 + 2\alpha + 4\beta)}\Phi_r \qquad (35)$$

Therefore, the air-gap magnetic flux density is:

$$B_g = \frac{A_m/A_g}{1 + \left(\frac{2R_g + R_s}{2R_{mo}}\right)(1 + 2\alpha + 4\beta)}B_r \qquad (36)$$

$$B_m = \frac{1 + \left(\frac{2R_g + R_s}{2R_{mo}}\right)(2\alpha + 4\beta)}{1 + \left(\frac{2R_g + R_s}{2R_{mo}}\right)(1 + 2\alpha + 4\beta)}B_r \qquad (37)$$

STEP 6.4. APPLYING PROPOSED QUASI-3D METHOD TO MEC

To apply the proposed MEC method to the AFPM machine, the quasi-3D method is employed. Each 2D model slice obtained using the quasi-3D method has a different value of w_f and w_m for each radius length. w_f and w_m for each slice model can be expressed as:

$$w_{f,i} = \frac{2\pi\theta_f}{360}r_i \qquad (38)$$

$$w_{m,i} = \frac{2\pi\theta_m}{360}r_i \qquad (39)$$

$$r_i = \frac{h}{n_s - 1}(i - 1) + \frac{D_{in}}{2} \qquad (40)$$

where i is a natural number from 1 to n_s.

The air-gap magnetic flux density varies according to the values of w_f and w_m. The air-gap magnetic flux density for each slice model $B_{g,i}$ can be expressed as:

$$B_{g,i} = \frac{A_{m,i}/A_{g,i}}{1 + \left(\frac{2R_{g,i} + R_{s,i}}{2R_{mo,i}}\right)(1 + 2\alpha_i + 4\beta_i)}B_r \qquad (41)$$

STEP 7. CONSIDERATION OF MAGNETIC SATURATION

Most of the magnetic saturation of the motor occurs in the stator, which leads to a significant deterioration in the performance of the machine. Therefore, based on the B-H curve data, the relative permeability $\mu_{rs}(B)$ is calculated using a PCHIP. A method of considering magnetic saturation is proposed by applying the calculated $\mu_{rs}(B)$ and the parameters calculated in step 6 to the proposed stator core permeability correction algorithm.
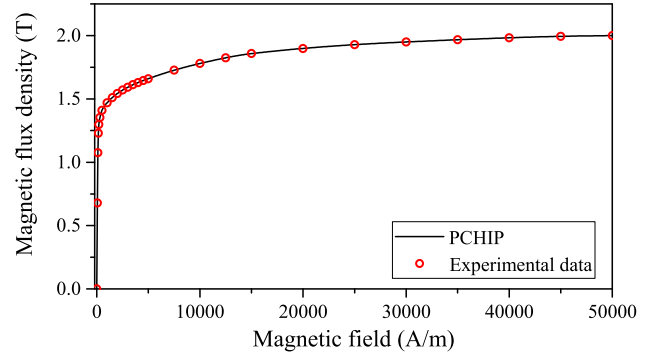

FIGURE 9. Comparison of the experimental B-H curve and a PCHIP.

TABLE 2. Coefficient of B-H curve polynomial using a PCHIP.

Interval of a	A_n	B_n	C_n	b_n
[0,100)	-1.1160E-07	-3.9840E-05	1.5850E-02	0
[100,150)	8.9839E-08	-3.3172E-05	4.5340E-03	1.075
[150,200)	-6.0688E-08	-7.5772E-06	1.1891E-03	1.230
[200,500)	1.3419E-09	-1.4171E-06	6.7769E-04	1.298
[500,1000)	1.5896E-10	-2.1896E-07	1.8974E-04	1.410
[1000,2500)	2.0504E-12	-1.8631E-08	9.0000E-05	1.470
[2500,5000)	8.6420E-13	-6.9392E-09	4.7947E-05	1.570
[5000,10000)	1.4545E-14	-1.1636E-09	2.9454E-05	1.660
[10000,15000)	-1.1187E-13	-1.0247E-10	1.8909E-05	1.780
[15000,30000)	3.7878E-15	-2.8087E-10	9.4942E-06	1.858
[30000,50000)	-2.3786E-15	-8.6670E-12	3.6248E-06	1.950

STEP 7.1. INTERPOLATION OF STATOR CORE PERMEABILITY FUNCTION

A PCHIP, an interpolation polynomial used in this paper, has the following characteristics [60].

1. It is a shape-preserving interpolation.

2. It seeks to match only the first-order derivatives at the data points with those of the intervals before and after.

3. The interpolation polynomial's minimum value matches the minimum value of the data.

4. On intervals where the data is monotonic, so are the interpolation polynomials.

5. It has no overshoots and less oscillation if the data is not smooth.

6. In general, a PCHIP curve does not have peaks and valleys. Curves can be differentiated at any point.

Therefore, it is an interpolation method suitable to be applied to a monotonic curve, such as the B-H curve, without peaks and valleys.

When the data are given as (a_n, b_n), where n is the number of data, the basic form of the polynomial obtained by applying a PCHIP $P(x)$ is as (42) where A, B, C, and D are coefficients obtained through a PCHIP.

In this paper, 12 B-H curve data points are used. Based on this, the functions obtained by applying a PCHIP using MATLAB are shown in Table II and Fig. 9, respectively.

Since the permeability is the slope of the B-H curve, the relative permeability of the material can be expressed as

$$\mu_{rs}(H) = \frac{1}{\mu_0}\frac{dB(H)}{dH} \qquad (43)$$

TABLE 3. Coefficient of Core permeability polynomial using a PCHIP.

Interval of a	A_n	B_n	C_n
[0,100)	-2.6642E-01	-63.4075	12613.02924
[100,150)	2.1447E-01	-52.7952	3608.05339
[150,200)	-1.4488E-01	-12.0595	1504.4781
[200,500)	3.2035E-03	-2.2554	539.2925
[500,1000)	3.7950E-04	-3.4849E-01	150.9912
[1000,2500)	4.8950E-06	-2.9652E-02	71.6197
[2500,5000)	2.0631E-06	-1.1044E-02	38.1548
[5000,10000)	3.4725E-08	-1.8520E-03	23.4392
[10000,15000)	-2.6707E-07	-1.6308E-04	15.0474
[15000,30000)	9.0427E-09	-4.4702E-04	7.5552
[30000,50000)	-5.6784E-09	-1.3794E-05	2.8845

TABLE 4. Coefficient of H-B curve polynomial using a PCHIP.

Interval of a	A_n	B_n	C_n	b_n
[0,1.075)	-1.6078E+01	1.0382E+02	0	0
[1.075,1.230)	-2.2049E+02	1.0349E+03	1.6747E+02	100
[1.230,1.298)	2.2602E+04	2.3292E+03	4.7240E+02	150
[1.298,1.410)	1.6627E+03	1.3884E+04	1.1027E+03	200
[1.410,1.470)	-5.3507E+05	9.9738E+04	4.2753E+03	500
[1.470,1.570)	4.8259E+03	4.4866E+04	1.0465E+04	1000
[1.570,1.660)	3.6464E+05	1.2387E+05	1.9583E+04	2500
[1.660,1.780)	6.6640E+04	6.4068E+04	3.3019E+04	5000
[1.780,1.858)	2.3021E+06	-1.5098E+04	5.1274E+04	10000
[1.858,1.950)	7.7252E+05	7.1269E+05	9.0937E+04	15000
[1.950,2.000)	-2.9950E+07	4.6638E+06	2.4169E+05	30000

Thus, the relative permeability function has the form of differentiating (42) and can be expressed as (44), as shown at the bottom of the page.

Therefore, the relative permeability function obtained by substituting the *B-H* curve function obtained through a PCHIP into (43) has the form of (44), and the coefficient of the function is shown in Table III.

The relative permeability function for the magnetic flux density $\mu_{rs}(B)$ is a composite of the inverse function of the *B-H* curve function $H(B)$ and the permeability function $\mu_{rs}(H)$, and is calculated as:

$$\mu_{rs}(B) = \mu_{rs}(H(B)) \quad (45)$$

where $H(B)$ has the same form as in (44), and each coefficient is shown in Table IV.

STEP 7.2. CALCULATION OF STATOR CORE PERMEABILITY OF SLOTLESS MOTOR

The core magnetic flux density of the slotless motor is obtained using the air-gap magnetic flux density obtained through the MEC analysis method proposed in Step 6. The core magnetic flux density $B_{s,slotless}$ is:

$$B_{s,slotless} = B_g \times \frac{A_g}{A_{s,slotless}} \quad (46)$$

where:

$$A_{s,slotless} = (w_m + w_f)L \quad (47)$$

Subsequently, the relative magnetic permeability of the core is updated by substituting the calculated $B_{s,slotless}$ to the relative permeability function $\mu_{rs}(B)$ obtained through (46), the core reluctance is recalculated, and the new air-gap magnetic flux density is calculated. Based on the newly calculated air-gap magnetic flux density, the relative permeability of the core is recalculated. This process is repeated until:

$$\mu_{rs}(B_{s,slotless}) = \mu_{rs,new}(B) \quad (48)$$

This algorithm is the stator core permeability correction algorithm proposed in this paper.

STEP 8. ANALYSIS OF SLOT OPENING EFFECT USING PROPOSED QUASI-3D METHOD

The analytical method proposed in steps 6 and 7 is a method targeting a slotless model. However, the model designed in this paper has a slot structure. Since the electromagnetic characteristics of the machine change depending on the existence of the slot, the analysis must be conducted in consideration of the slot opening effect.

In this step, two methods are used to consider the slot opening effect. First, a method of calculating the slot opening effect coefficient of the AFPM motor by combining the quasi-3D method with a complex function-based conformal transformation is proposed.

Second, to consider the concentration of magnetic flux occurring in the slot, a method of calculating the flux concentration coefficient of the AFPM motor by combining the method using the ratio of the slot opening area and the tooth area with the quasi-3D method is proposed.

$$P(x) = \begin{cases} A_1(x-a_1)^3 + B_1(x-a_1)^2 + C_1(x-a_1) + b_1 & at\ a_1 \le x < a_2 \\ A_2(x-a_2)^3 + B_2(x-a_2)^2 + C_2(x-a_2) + b_2 & at\ a_2 \le x < a_3 \\ \vdots \\ A_{n-1}(x-a_{n-1})^3 + B_{n-1}(x-a_{n-1})^2 + C_{n-1}(x-a_{n-1}) + b_{n-1} & at\ a_{n-1} \le x < a_n \end{cases} \quad (42)$$

$$\frac{dP(x)}{dx} = \begin{cases} A_1(x-a_1)^2 + B_1(x-a_1) + C_1 & at\ a_1 \le x < a_2 \\ A_2(x-a_2)^2 + B_2(x-a_2) + C_2 & at\ a_2 \le x < a_3 \\ \vdots \\ A_{n-1}(x-a_{n-1})^2 + B_{n-1}(x-a_{n-1}) + C_{n-1} & at\ a_{n-1} \le x < a_n \end{cases} \quad (44)$$
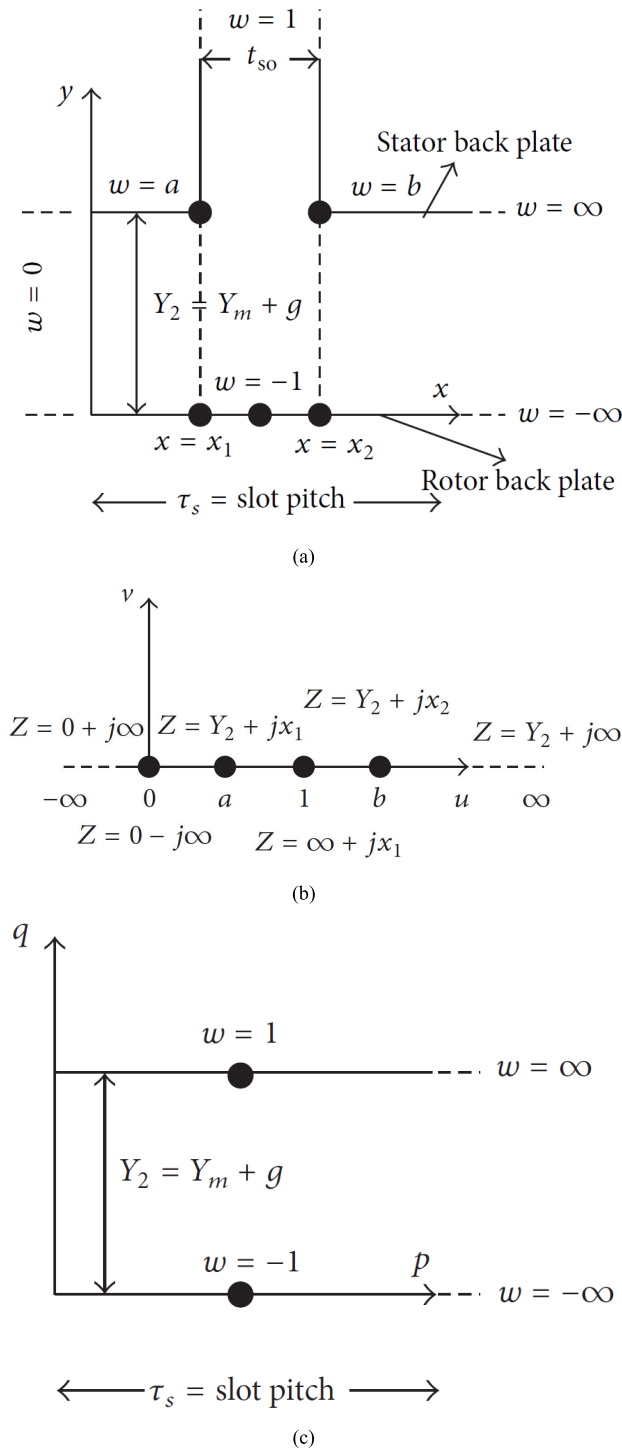
(a)

(b)

(c)

FIGURE 10. Slot opening of the AFPM machine (a) in the z-plane, (b) in the w-plane, (c) in the t-plane.

STEP 8.1. DETERMINATION OF SLOT OPENING EFFECT COEFFICIENT

The conformal transformation for the AFPM machine proceeds through the transformation of three planes: the z-, w-, and t-planes [48], [61]. The slot opening in each plane is shown in Fig. 10.

The first transformation, the conformal transformation from the z-plane to the w-plane, is also known as the Schwarz-Christoffel transformation. The equation for z-w conformal transformation is:

$$\frac{dz}{dw} = A(w-a)^{(\alpha/\pi)-1}(w-b)^{(\beta/\pi)-1}(w-c)^{(\gamma/\pi)-1}\cdots \tag{49}$$

The equation for the z-w conformal transformation of the AFPM motor obtained using (49) is:

$$\frac{dz}{dw} = j\frac{Y_2}{\pi}\frac{(w-a)^{1/2}(w-b)^{1/2}}{w(w-1)} \tag{50}$$

where coefficient a and b is:

$$b = \left[\frac{t_{so}}{2Y_2} + \sqrt{\left(\frac{t_{so}}{2Y_2}\right)^2 + 1}\right]^2 \tag{51}$$

$$a = \frac{1}{b} \tag{52}$$

If $p^2 = (w-b)/(w-a)$ is defined, (50) can be derived as:

$$z = j\frac{2Y_2}{\pi}\int\frac{(b+1)^2(b-1)p^2}{(1-p^2)(b^2-p^2)(b+p^2)}dp \tag{53}$$

$$z = j\frac{Y_2}{\pi}\left(\ln\left[\frac{1+p}{1-p}\right] - \ln\left[\frac{b+p}{b-p}\right] - \frac{2(b-1)}{\sqrt{b}}\tan^{-1}\frac{p}{\sqrt{b}}\right) + C \tag{54}$$

By substituting w = b for (54), the integral constant C can be calculated as:

$$C = Y_2 + jx_2 \tag{55}$$

The second conformal transformation is from the w-plane to the t-plane, and the equation is:

$$\frac{dt}{dw} = \frac{A}{w}dw \tag{56}$$

The equation for the w-t conformal transformation of the AFPM motor obtained using (56) is:

$$t = j\frac{Y_2}{\pi}w + Y_2 + j\frac{\tau_s}{2} = q + jp \tag{57}$$

Therefore, the slot opening effect coefficient can be calculated using (54) and (57) as:

$$\lambda = \frac{\partial t}{\partial z} = \frac{\partial t}{\partial w}\frac{\partial w}{\partial z} = \frac{(w-1)}{(w-a)^{1/2}(w-b)^{1/2}} \tag{58}$$

This slot opening effect coefficient is also known as the relative air-gap permeance. The slot opening effect coefficient for the azimuth angle of the AFPM motor is shown in Fig. 11.

STEP 8.2. APPLYING QUASI-3D METHOD TO SLOT OPENING EFFECT COEFFICIENT

To apply the calculated slot opening effect coefficient to the AFPM machine, a novel slot opening effect coefficient calculation method combined with the quasi-3D method is proposed. Each 2D model slice obtained using the quasi-3D
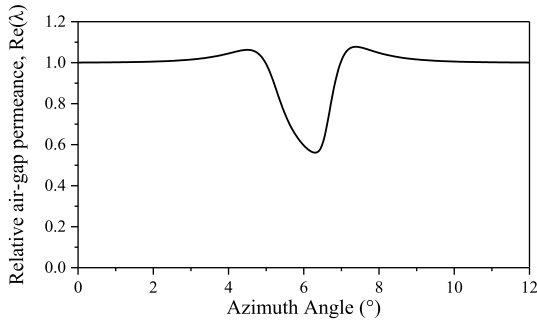
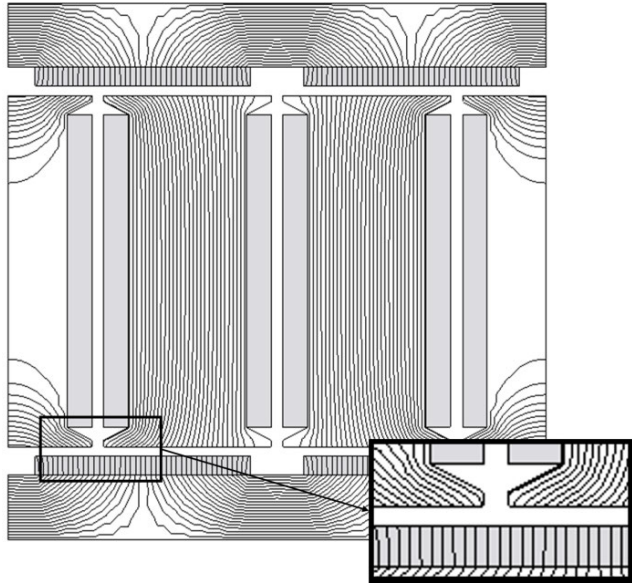**FIGURE 11.** Slot opening effect coefficient graph.

FIGURE 12. Flux flow line graph of the AFPM motor.

method has a different value of x_2 for each radius length. x_2 can be expressed as:

$$x_{2,i} = \frac{x_{2,R_{in}} - x_{2,R_{out}}}{h} l_i + x_{2,R_{out}} \qquad (59)$$

where $x_{2,R_{in}}$ is the value of x_2 of the 2D model sliced with the inner radius length of the designed AFPM motor, and $x_{2,R_{out}}$ is the value of x_2 of the 2D model sliced with the outer radius length of the designed AFPM motor.

Therefore, the slot opening effect coefficient of the *i-th* slice model λ_i is:

$$\lambda_i = \frac{\partial t}{\partial z} = \frac{(w_i - 1)}{(w_i - a)^{1/2}(w_i - b)^{1/2}} \qquad (60)$$

STEP 8.3. DETERMINATION OF FLUX CONCENTRATION COEFFICIENT

Fig. 12 shows the graph of the magnetic flux flow of the AFPM motor. In the slot model, the magnetic flux is concentrated in the tooth segment, which has a reluctance smaller than that of the slot opening segment. In this step, a method is proposed to consider the effect caused by magnetic concentration [49].

Fig. 13 is an equivalent model proposed to consider the magnetic flux concentration phenomenon occurring in the
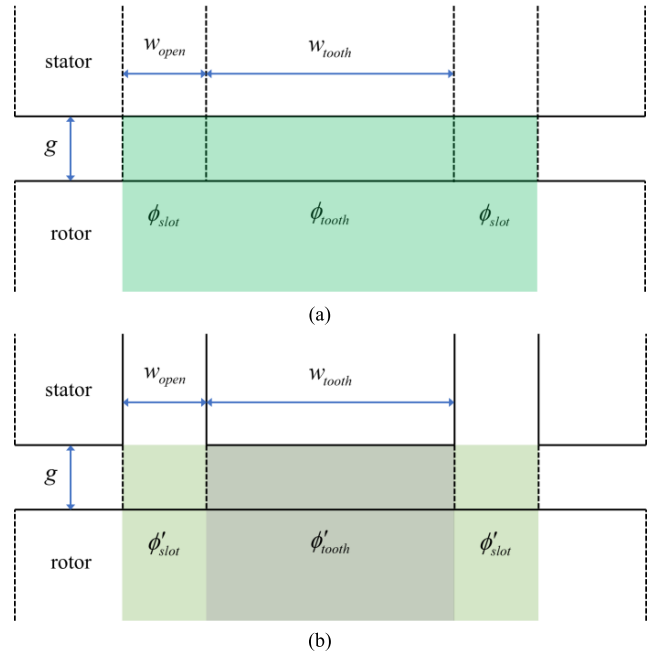
FIGURE 13. Equivalent model of the magnetic flux concentration effect consideration in (a) slotless AFPM motor (b) slotted AFPM motor.

AFPM motor. By calculating the ratio of each region to the total magnetic flux through Fig. 13(a), the magnetic flux of the slot opening segment and the magnetic flux of the tooth segment of the slotless model can be calculated as:

$$\phi_{slot} = \phi_{rotor} \cdot \frac{w_{open}}{w_{open} + w_{tooth}} \qquad (61)$$

$$\phi_{tooth} = \phi_{rotor} \cdot \frac{w_{tooth}}{w_{open} + w_{tooth}} \qquad (62)$$

From Fig. 13(b), (61), and (62), the magnetic flux of the slot opening segment and of the tooth segment of the slot model can be calculated as follows:

$$\phi'_{slot} = \phi_{slot} \cdot \lambda_{ave} \qquad (63)$$

$$\phi'_{tooth} = \phi_{rotor} - \phi'_{slot} \qquad (64)$$

where λ_{ave} is the average relative air-gap permeance and is calculated as:

$$\lambda_{ave} = \frac{1}{w_{open}} \sum_{w_{open}} Re\{\lambda(x)\} \qquad (65)$$

Therefore, the flux concentration coefficient is calculated as:

$$k_{con} = \frac{\phi'_{tooth}}{\phi_{tooth}} \qquad (66)$$

STEP 8.4. APPLYING QUASI-3D METHOD TO FLUX CONCENTRATION COEFFICIENT

To apply the calculated magnetic flux concentration coefficient to the AFPM machine, a novel magnetic flux concentration coefficient calculation method combining the quasi-3D method is proposed. Each 2D model slice obtained using

the quasi-3D method has a different value of w_{tooth} for each radius length. w_{tooth} can be expressed as:

$$w_{tooth} = \frac{w_{so} - w_{si}}{h} l_i + w_{so} \tag{67}$$

In addition, since λ_{ave} is different for each 2D model slice by (60) and (65), λ_{ave} for each i-th 2D model is expressed as:

$$\lambda_{ave,i} = \frac{1}{w_{open}} \sum_{w_{open}} Re\{\lambda_i(x)\} \tag{68}$$

Therefore, the flux concentration coefficient $k_{con,i}$ for each i-th slice 2D model can be expressed as:

$$k_{con,i} = \frac{\phi'_{tooth,i}}{\phi_{tooth,i}} \tag{69}$$

STEP 9. CALCULATION OF MAGNETIC FLUX DENSITY OF THE SLOTTED MOTOR

The air-gap magnetic flux density of the AFPM motor $B_{g,slotted}$ calculated by applying the analysis method proposed in Steps 6, 7, and 8 is:

$$B_{g,slotted} = \frac{1}{n_s} \sum_{i=1}^{n_s} B_{g,i} \times Re(\lambda_i) \times k_{con,i} \tag{70}$$

where n_s is the number of slices, and the larger n_s is, the higher the accuracy. However, the analysis time also increases, so an appropriate value should be selected according to the designer's environment.

Next, two things are checked to make sure that the correct design is performed. First, the core magnetic flux density of the slotted model $B_{s,slotted}$ is compared with the maximum allowable core magnetic flux density $B_{s,max}$. The core magnetic flux density of the slotted model $B_{s,slot}$ is calculated as:

$$B_{s,slotted} = B_{g,slotted} \times \frac{A_g}{A_{s,slot}} \tag{71}$$

where $A_{s,slot}$ is the cross-sectional area of the stator tooth in the slotted model.

If $B_{s,slotted}$ is larger than $B_{s,max}$, magnetic saturation will occur and the efficiency will be significantly reduced, so the design must be changed.

Second, whether $B_{g,slotted}$ is satisfied with the design target performance is checked by comparing $B_{g,slotted}$ and the target air-gap magnetic flux density $B_{designed}$.

The results of applying the proposed analysis method to the AFPM motor designed in this paper are confirmed in Figs. 14 and 15.

When compared with the results obtained through 3D FEA, the error from the proposed analytical method is less than 1%, and the analysis time is approximately 20 seconds, which is much faster than 3D FEA. Therefore, the proposed analytical method has very high accuracy and analysis speed; thus, it is practicable and can be applied to the AFPM motor design.
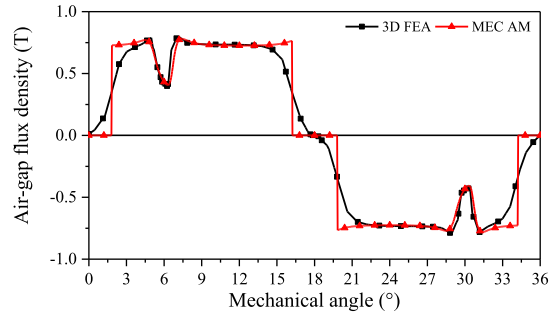

FIGURE 14. The air-gap flux density using the proposed analytical method.
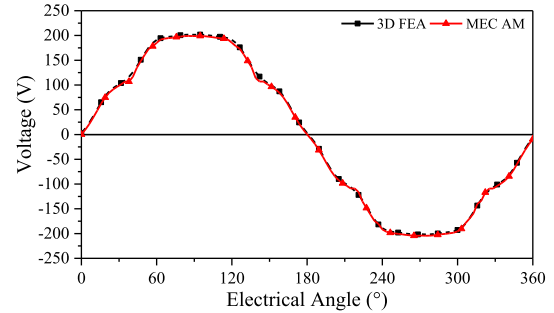

FIGURE 15. The Back EMF of the AFPM motor using the proposed analytical method.

C. FEA OF THE DESIGNED MOTOR

To determine the parameters of the AFPM motor designed through stages A and B, which cannot be obtained through analytical methods, such as the reduction of cogging torque, and to obtain all the characteristics of the designed motor to verify that it is designed correctly, FEA of the motor is conducted using JMAG, a commercial tool of proven accuracy.

STEP 10. APPLYING COGGING TORQUE REDUCTION TECHNIQUE

Cogging torque is the force that the rotor applies to align in the direction of minimum reluctance during no-load operation and is caused by the difference in reluctance between the stator slot and the rotor permanent magnet. This is the parameter that must be minimized, as it lowers the control precision of the machine and causes vibration and noise.

There are many ways to reduce the cogging torque, but in this paper, the most representative method—magnet skewing—is used. Magnet skewing is a method of skewing the shape of a magnet by a certain angle as shown in Fig. 16.

The smallest skew angle that minimizes the cogging torque is shown in [62] as:

$$\theta_{skew} = \frac{2\pi}{N_c} \tag{72}$$

where N_s is the number of motor slots.

However, (72) is an equation for an RFPM machine in general, and the optimum skew angle is different from (72), as the inner and outer radii of an AFPM machine are different. Therefore, it is necessary to find the optimal skew angle of the designed model by obtaining the magnitude of the
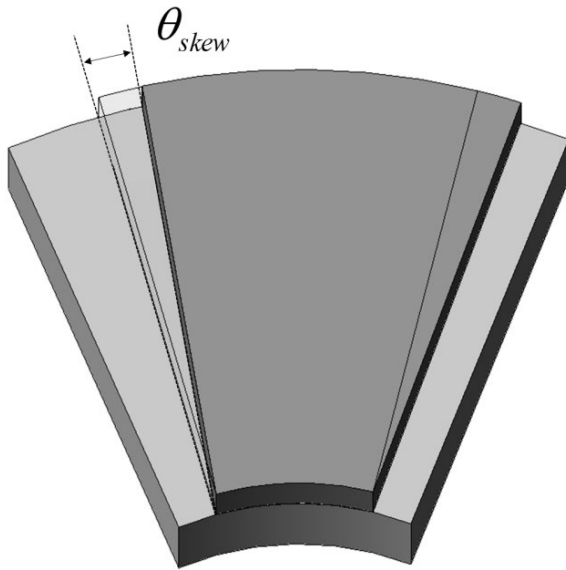
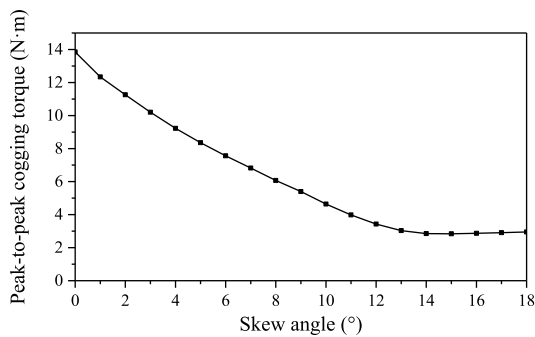FIGURE 16. Magnet skewing of the AFPM machine rotor.

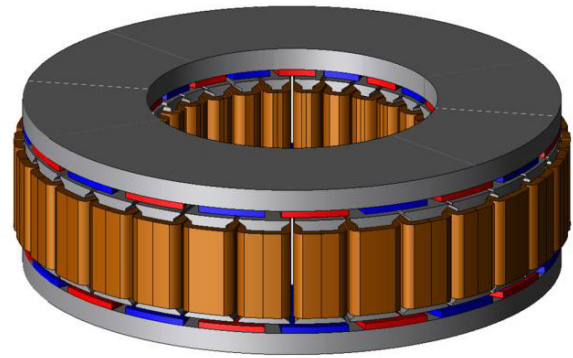FIGURE 17. Variation of the peak-to-peak cogging torque with skew angle.

FIGURE 18. Designed AFPM motor structure.
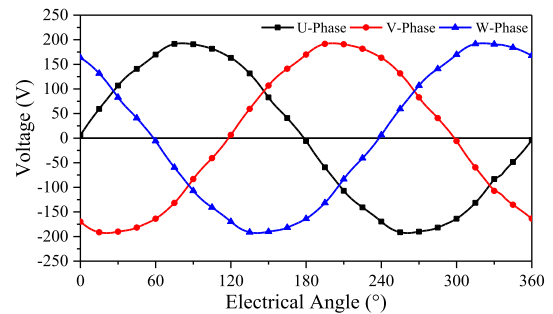

FIGURE 19. The Back EMF of the AFPM motor using 3D FEA.
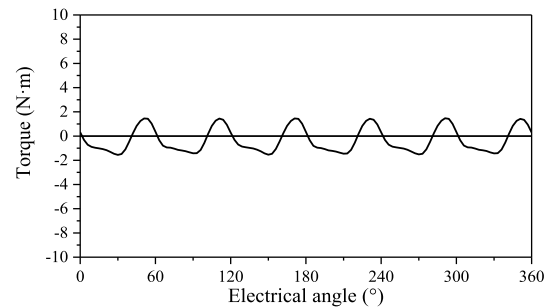
FIGURE 20. The cogging torque of the AFPM motor using 3D FEA.

peak-to-peak cogging torque based on the skew angle. The results are shown in Fig. 17, and based on this, the final skew angle was determined to be 15°.

STEP 11. FEA OF ELECTROMAGNETIC CHARACTERISTICS OF THE DESIGNED MOTOR

In this step, FEA is conducted to determine the electromagnetic characteristics of the designed motor in the no-load and load conditions and to check whether the motor is designed to satisfy the requirements. Fig. 18 shows the structure of an AFPM motor designed using the process proposed in this paper.

STEP 11.1. NO-LOAD ANALYSIS USING FEA

In the no-load analysis, the back EMF of the motor, THD of the back EMF, and cogging torque can be obtained. This analysis was conducted at a base speed of 2,400 rpm. The back EMF is the voltage induced in the no-load operation. When a Fourier transform is applied to the back EMF waveform,

harmonics can be obtained, and the THD is calculated as:

$$THD = \frac{\sqrt{V_2^2 + V_3^2 + V_4^2 + \cdots}}{V_1} \qquad (73)$$

Fig. 19 shows the back EMF waveform of the designed motor. The THD of the designed motor is very small, approximately 2.3%. The smaller the THD, the closer the waveform is to a sine wave, which means that heat, vibration, and core loss of the motor are reduced, improving the performance of the motor.

Fig. 20 shows the magnitude of the cogging torque of the designed motor, which was also very small, approximately 3.02 N·m.

Fig. 21 shows the magnetic flux density distribution in the no-load state of the designed AFPM motor. The maximum magnetic flux density was approximately 1.2 T, confirming that the motor had been designed correctly. The maximum
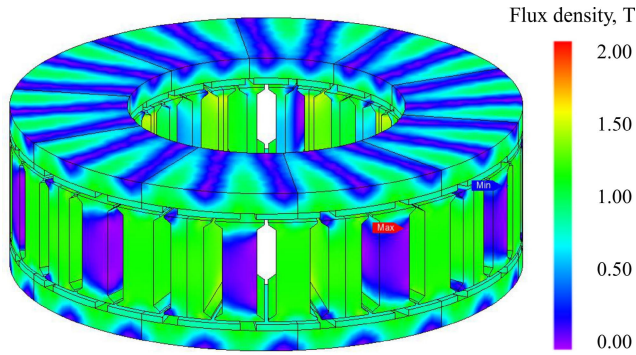
FIGURE 21. The no-load magnetic flux density distribution of the designed AFPM motor.
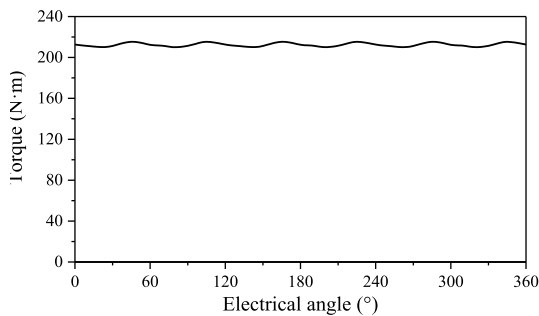

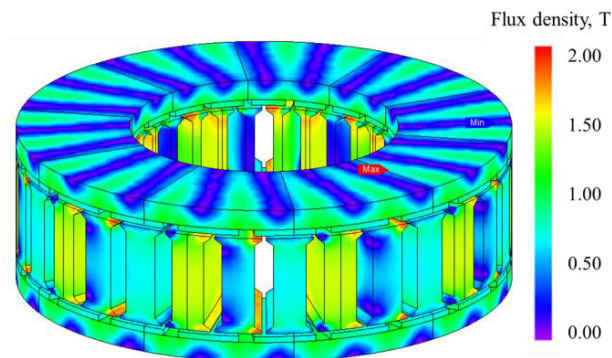**FIGURE 22.** The load torque of the AFPM motor using 3D FEA.

**FIGURE 23.** The load magnetic flux density distribution of the designed AFPM motor.

magnetic flux density was also small enough to not have to consider magnetic saturation.

STEP 11.2. LOAD ANALYSIS USING FEA
In the load analysis, the torque, power, torque ripple, and efficiency of the motor can be obtained. This analysis was conducted at a base speed of 2,400 rpm.

Fig. 22 shows the load torque and torque ripple magnitude of the designed motor. The designed motor had a torque of 212 N·m and a torque ripple of approximately 4.7%. This was more than the target torque size of 200 N·m and less than a torque ripple target of 5% (or less), confirming that the motor had been designed correctly.

Fig. 23 shows the distribution of magnetic flux density in the loaded state of the designed AFPM motor. The maximum magnetic flux density was about 2.1 T, which was large
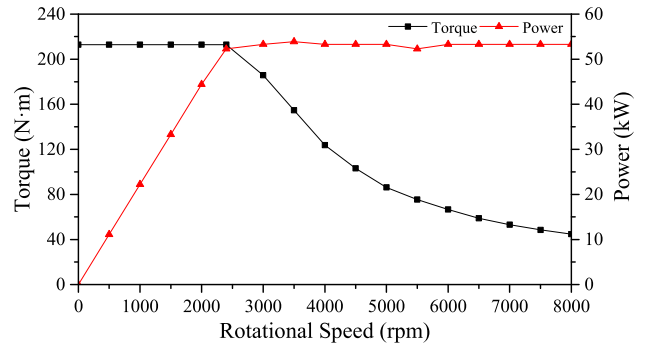
(a)
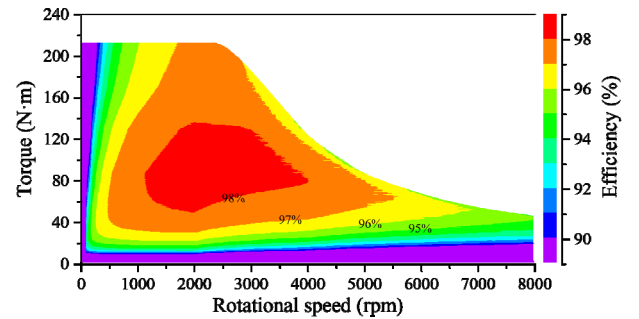
(b)

FIGURE 24. (a) The speed-torque-power curve and (b) efficiency map of the designed AFPM motor.

TABLE 5. Parameters of the AFPM motor for an in-wheel system.

Parameter	Value	Unit
Pole/Slot number	20/30	-
Outer diameter	240	mm
Inner diameter	130	mm
Axial length	74	mm
Air-gap length	1.5	mm
Magnet thickness	3	mm
Pole-arc ratio	0.8	-
Skew angle	15	°
Rotor thickness	8	mm
Coil diameter	4	mm
Slot width	9	mm
Slot opening width	2	mm
Maximum power	53	kW
Maximum torque	212	N·m
Base speed	2400	rpm
Maximum efficiency	98.2	%
Torque ripple	4.7	%
THD	2.3	%

enough to consider magnetic saturation. However, it occurred only in parts of the stator teeth and had a relatively low magnetic flux density in the main flux path. As such, the performance reduction due to magnetic saturation was very small.

Fig. 24 shows the speed-torque-power characteristic and efficiency map of the AFPM motor calculated by FEA under the load condition. The maximum efficiency of the motor was 98.2% at 2,000 rpm, confirming that the designed motor had very high efficiency.

STEP 12. CONFIRMING THE FINAL PARAMETERS OF THE DESIGNED MOTOR

The parameters and characteristics of the motor designed in this paper are shown in Table V.

The motor designed satisfies the requirements of an electric vehicle in-wheel system motor, such as a maximum torque of 212 N·m, maximum power of 53 kW, maximum efficiency of 98.2%, and a wide high-efficiency operating range. In addition, through electromagnetic analysis, the motor was designed correctly by having a torque ripple of approximately 4.7%, a low core magnetic flux density that did not require magnetic saturation be considered, and a THD of approximately 2.3%.

III. CONCLUSION

As the interest in eco-friendly technology increases daily, the demand for electric vehicles increases. Therefore, this paper presents an AFPM motor analysis and design method for use in an in-wheel system that is suitable for electric vehicles.

When designing an AFPM motor, it is difficult to estimate the exact outer diameter of the motor and the shape of the coil windings because of the clearance distance required by the end-winding. Therefore, it is noteworthy that a novel analytical method can precisely estimate the outer diameter and the shape of the coil winding as proposed in this paper, making it possible to effectively design the housing and cooling system of such a motor.

An AFPM motor inevitably needs to perform 3D FEA due to its structural characteristics, which requires significant time and expense in its analysis. Therefore, this paper has significant implications in that respect, proposing a novel analytical method combined with a numerical method, which considers not only the motor's 3D structural effects but also its complex geometry and can reduce both the development time and cost of an AFPM motor.

Due to the nonlinearity of the magnetic saturation in the core, it is difficult to consider it in the analysis, and thus it lowers the analysis accuracy. Remarkably, the novel algorithm and analytical method proposed in this paper can consider the magnetic saturation with high accuracy.

An in-wheel motor requires a high torque density and efficiency within the context of a small volume and compact shape. In this respect, it is noteworthy that the motor designed using the proposed analysis and design method improved torque density and efficiency, compared with conventional RFPM motors, and significantly reduced the energy consumption and motor volume, thus satisfying the requirements for the in-wheel system of electric vehicles.

The proposed analysis and design method can be applied to AFPM motors as well as to a diverse array of electrical machines.

In our future work, we will add stress analysis to verify the reliability of the designed motor, and manufacture a prototype motor to experimentally verify and supplement the reliability of the proposed analytical method. In addition, AFPM motors are more prone to failure than RFPM motors owing to their structural characteristics. Therefore, we will aim to study the fault detection and diagnostic control applicable to AFPM motors.

REFERENCES

[1] L. Guo, P. Ge, and D. Sun, "Torque distribution algorithm for stability control of electric vehicle driven by four in-wheel motors under emergency conditions," *IEEE Access*, vol. 7, pp. 104737–104748, 2019.

[2] K. Sone, M. Takemoto, S. Ogasawara, K. Takezaki, and H. Akiyama, "A ferrite PM in-wheel motor without rare Earth materials for electric city commuters," *IEEE Trans. Magn.*, vol. 48, no. 11, pp. 2961–2964, Nov. 2012.

[3] Y.-P. Yang and D. S. Chuang, "Optimal design and control of a wheel motor for electric passenger cars," *IEEE Trans. Magn.*, vol. 43, no. 1, pp. 51–61, Jan. 2007.

[4] S. P. Nikam, V. Rallabandi, and B. G. Fernandes, "A High-Torque-Density permanent-magnet free motor for in-wheel electric vehicle application," *IEEE Trans. Ind. Appl.*, vol. 48, no. 6, pp. 2287–2295, Nov. 2012.

[5] T. Li, Y. Zhang, Y. Liang, Q. Ai, and H. Dou, "Multiphysics analysis of an axial-flux in-wheel motor with an amorphous alloy stator," *IEEE Access*, vol. 8, pp. 27414–27425, 2020.

[6] S. Kahourzade, A. Mahmoudi, H. W. Ping, and M. N. Uddin, "A comprehensive review of axial-flux permanent-magnet machines," *Can. J. Electr. Comput. Eng.*, vol. 37, no. 1, pp. 19–33, 2014.

[7] T. Takahashi, M. Takemoto, S. Ogasawara, W. Hino, and K. Takezaki, "Size and weight reduction of an in-wheel axial-gap motor using ferrite permanent magnets for electric commuter cars," *IEEE Trans. Ind. Appl.*, vol. 53, no. 4, pp. 3927–3935, Jul. 2017.

[8] M. Lehr, K. Reis, and A. Binder, "Vergleich von Axial- und Radialfluss-Maschinen für den Einsatz in Radnabenantrieben," *Elektrotechnik und Informationstechnik*, vol. 132, no. 1, pp. 25–32, Feb. 2015.

[9] N. Salim, S. P. Nikam, S. Pal, A. K. Wankhede, and B. G. Fernandes, "Multiphysics analysis of printed circuit board winding for high-speed axial flux permanent magnet motor," *IET Electr. Power Appl.*, vol. 13, no. 6, pp. 827–832, 2019.

[10] Z. Makni, M. Besbes, and C. Marchand, "Multiphysics design methodology of permanent-magnet synchronous motors," *IEEE Trans. Veh. Technol.*, vol. 56, no. 4, pp. 1524–1530, Jul. 2007.

[11] F. L. M. dos Santos, J. Anthonis, F. Naclerio, J. J. C. Gyselinck, H. Van der Auweraer, and L. C. S. Goes, "Multiphysics NVH modeling: Simulation of a switched reluctance motor for an electric vehicle," *IEEE Trans. Ind. Electron.*, vol. 61, no. 1, pp. 469–476, Jan. 2014.

[12] S.-I. Kim, S. Park, T. Park, J. Cho, W. Kim, and S. Lim, "Investigation and experimental verification of a novel spoke-type ferrite-magnet motor for electric-vehicle traction drive applications," *IEEE Trans. Ind. Electron.*, vol. 61, no. 10, pp. 5763–5770, Oct. 2014.

[13] W.-H. Kim, I.-S. Jang, C.-S. Jin, J. Lee, and S.-G. Lee, "Design of novel overhang structure for separated pole-piece type ferrite magnet motor," *IEEE Trans. Magn.*, vol. 51, no. 3, pp. 1–4, Mar. 2015.

[14] Z. Wang, R. Masaki, S. Morinaga, Y. Enomoto, H. Itabashi, M. Ito, and S. Tanigawa, "Development of an axial gap motor with amorphous metal cores," *IEEE Trans. Ind. Appl.*, vol. 47, no. 3, pp. 1293–1299, May 2011.

[15] K. Zhang, B. Jiang, X.-G. Yan, and Z. Mao, "Incipient fault detection for traction motors of high-speed railways using an interval sliding mode observer," *IEEE Trans. Intell. Transp. Syst.*, vol. 20, no. 7, pp. 2703–2714, Jul. 2019.

[16] Y. Wu, B. Jiang, N. Lu, H. Yang, and Y. Zhou, "Multiple incipient sensor faults diagnosis with application to high-speed railway traction devices," *ISA Trans.*, vol. 67, pp. 183–192, Mar. 2017.

[17] Y. Wu, B. Jiang, and Y. Wang, "Incipient winding fault detection and diagnosis for squirrel-cage induction motors equipped on CRH trains," *ISA Trans.*, vol. 99, pp. 488–495, Apr. 2020.

[18] Y. Wu, B. Jiang, and N. Lu, "A descriptor system approach for estimation of incipient faults with application to high-speed railway traction devices," *IEEE Trans. Syst., Man, Cybern. Syst.*, vol. 49, no. 10, pp. 2108–2118, Oct. 2019.

[19] S. Huang, J. Luo, F. Leonardi, and T. A. Lipo, "A comparison of power density for axial flux machines based on general purpose sizing equations," *IEEE Power Eng. Rev.*, vol. 17, no. 11, p. 55, Mar. 1997.

[20] J. A. Tapia, M. Aydin, S. Huang, and T. A. Lipo, "Sizing equation analysis for field controlled PM machines: A unified approach," in *Proc. IEEE Int. Electr. Mach. Drives Conf.*, vol. 2, Jun. 2003, pp. 1111–1116.

[21] A. Mahmoudi, S. Kahourzade, N. A. Rahim, and W. P. Hew, "Design, analysis, and prototyping of an axial-flux permanent magnet motor based on genetic algorithm and finite-element analysis," *IEEE Trans. Magn.*, vol. 49, no. 4, pp. 1479–1492, Apr. 2013.

[22] S. Huang, J. Luo, F. Leonardi, and T. A. Lipo, "A general approach to sizing and power density equations for comparison of electrical machines," *IEEE Trans. Ind. Appl.*, vol. 34, no. 1, pp. 92–97, 1998.

[23] A. Mahmoudi, N. A. Rahim, and H. W. Ping, "Axial-flux permanent-magnet motor design for electric vehicle direct drive using sizing equation and finite element analysis," *Prog. Electromagn. Res.*, vol. 122, pp. 467–496, 2012.

[24] A. Cavagnino, M. Lazzari, F. Profumo, and A. Tenconi, "A comparison between the axial flux and the radial flux structures for PM synchronous motors," *IEEE Trans. Ind. Appl.*, vol. 38, no. 6, pp. 1517–1524, Nov. 2002.

[25] T. Merzouki, A. Duval, and T. Ben Zineb, "Finite element analysis of a shape memory alloy actuator for a micropump," *Simul. Model. Pract. Theory*, vol. 27, pp. 112–126, Sep. 2012.

[26] W. Zhao, F. Xing, X. Wang, T. A. Lipo, and B. Il Kwon, "Design and analysis of a novel PM-assisted synchronous reluctance machine with axially integrated magnets by the finite-element method," *IEEE Trans. Magn.*, vol. 53, no. 6, Jun. 2017, Art. no. 8104104.

[27] J. Zhao, W. Fu, Y. Zheng, Z. Chen, and Y. Wang, "Comparative study of modular-stator and conventional outer-rotor flux-switching permanent-magnet motors," *IEEE Access*, vol. 7, pp. 38297–38305, 2019.

[28] H.-K. Yeo and J. Ro, "Novel analytical method for overhang effects in surface-mounted permanent-magnet machines," *IEEE Access*, vol. 7, pp. 148453–148461, 2019.

[29] D. Vanoost, H. De Gersem, J. Peuteman, G. Gielen, and D. Pissoort, "Two-dimensional magnetostatic finite-element simulation for devices with a radial symmetry," *IEEE Trans. Magn.*, vol. 50, no. 5, pp. 1–4, May 2014.

[30] A. Parviainen, M. Niemela, and J. Pyrhonen, "Modeling of axial flux PM machines," in *Proc. IEEE Int. Electr. Mach. Drives Conf. (IEMDC)*, Jun. 2003, vol. 3, no. 5, pp. 1955–1961.

[31] W. Tong, S. Wang, S. Dai, S. Wu, and R. Tang, "A Quasi-Three-Dimensional magnetic equivalent circuit model of a double-sided axial flux permanent magnet machine considering local saturation," *IEEE Trans. Energy Convers.*, vol. 33, no. 4, pp. 2163–2173, Dec. 2018.

[32] R. Qu and T. A. Lipo, "Analysis and modeling of air-gap and zigzag leakage fluxes in a surface-mounted permanent-magnet machine," *IEEE Trans. Ind. Appl.*, vol. 40, no. 1, pp. 121–127, Jan. 2004.

[33] A. Daghigh, H. Javadi, and H. Torkaman, "Considering wind speed characteristics in the design of a coreless AFPM synchronous generator," *Int. J. Renew. Energy Res.*, vol. 6, no. 1, pp. 263–270, 2016.

[34] A. Daghigh, H. Javadi, and A. Javadi, "Improved analytical modeling of permanent magnet leakage flux in design of the coreless axial flux permanent magnet Generatorx," *Can. J. Elect. Comput. Eng.*, vol. 40, no. 1, pp. 3–11, 2017.

[35] A. Daghigh, H. Javadi, and H. Torkaman, "Design optimization of direct-coupled ironless axial flux permanent magnet synchronous wind generator with low cost and high annual energy yield," *IEEE Trans. Magn.*, vol. 52, no. 9, pp. 1–11, Sep. 2016.

[36] A. Daghigh, H. Javadi, and H. Torkaman, "Optimal design of coreless axial flux permanent magnet synchronous generator with reduced cost considering improved PM leakage flux model," *Electr. Power Compon. Syst.*, vol. 45, no. 3, pp. 264–278, Feb. 2017.

[37] J. Y. Song, J. H. Lee, D. W. Kim, Y. J. Kim, and S.-Y. Jung, "Analysis and modeling of permanent magnet variable flux memory motors using magnetic equivalent circuit method," *IEEE Trans. Magn.*, vol. 53, no. 11, Nov. 2017, Art. no. 8208905.

[38] R. Benlamine, F. Dubas, S.-A. Randi, D. Lhotellier, and C. Espanet, "Modeling of an axial-flux interior PMs machine for an automotive application using magnetic equivalent circuit," in *Proc. 18th Int. Conf. Electr. Mach. Syst. (ICEMS)*, Pattaya, Thailand, Oct. 2015, pp. 1266–1271.

[39] N. Gabdullin and J. Ro, "Novel non-linear transient path energy method for the analytical analysis of the non-periodic and non-linear dynamics of electrical machines in the time domain," *IEEE Access*, vol. 7, pp. 37833–37854, 2019.

[40] A. Abdallh, G. Crevecoeur, and L. Dupré, "Optimal needle placement for the accurate magnetic material quantification based on uncertainty analysis in the inverse approach," *Meas. Sci. Technol.*, vol. 21, no. 11, Nov. 2010, Art. no. 115703.

[41] A. A.-E. Abdallh, P. Sergeant, G. Crevecoeur, L. Vandenbossche, L. Dupre, and M. Sablik, "Magnetic material identification in geometries with non-uniform electromagnetic fields using global and local magnetic measurements," *IEEE Trans. Magn.*, vol. 45, no. 10, pp. 4157–4160, Oct. 2009.

[42] J. Bao, B. L. J. Gysen, and E. A. Lomonova, "Hybrid analytical modeling of saturated linear and rotary electrical machines: Integration of Fourier modeling and magnetic equivalent circuits," *IEEE Trans. Magn.*, vol. 54, no. 11, Nov. 2018, Art. no. 8109905.

[43] P. Diez and J. P. Webb, "A rational approach to $B - -H$ curve representation," *IEEE Trans. Magn.*, vol. 52, no. 3, Mar. 2016, Art. no. 7203604.

[44] Y. Han, S. Chen, C. Gao, M. Gao, J. Si, and Y. Hu, "Effect of slot opening width on the air-gap magnetic field of a direct drive permanent magnet motor," *Appl. Sci.*, vol. 9, no. 21, p. 4649, Nov. 2019.

[45] J. H. Choi, "Design of high power permanent magnet motor with segment rectangular copper wire and closed slot opening on electric vehicles," *IEEE Trans. Magn.*, vol. 46, no. 9, pp. 3701–3704, Jun. 2010.

[46] J. Wanjiku, M. A. Khan, P. S. Barendse, and P. Pillay, "Influence of slot openings and tooth profile on cogging torque in axial-flux PM machines," *IEEE Trans. Ind. Electron.*, vol. 62, no. 12, pp. 7578–7589, Dec. 2015.

[47] D. Zarko, D. Ban, and T. A. Lipo, "Analytical calculation of magnetic field distribution in the slotted air gap of a surface permanent-magnet motor using complex relative air-gap permeance," *IEEE Trans. Magn.*, vol. 42, no. 7, pp. 1828–1837, Jul. 2006.

[48] A. Hemeida and P. Sergeant, "Analytical modeling of surface PMSM using a combined solution of Maxwell–s equations and magnetic equivalent circuit," *IEEE Trans. Magn.*, vol. 50, no. 12, Dec. 2014, Art. no. 7027913.

[49] D.-K. Lim and J. Ro, "Analysis and design of a delta-type interior permanent magnet synchronous generator by using an analytic method," *IEEE Access*, vol. 7, pp. 85139–85145, 2019.

[50] N. A. Rahim, H. W. Ping, and M. Tadjuddin, "Design of axial flux permanent magnet brushless DC motor for direct drive of electric vehicle," in *Proc. IEEE Power Eng. Soc. Gen. Meeting*, Jun. 2007, pp. 1–6.

[51] F. Caricchi, F. G. GiuliiCapponi, F. Crescimbini, and L. Solero, "Experimental study on reducing cogging torque and no-load power loss in axial-flux permanent-magnet machines with slotted winding," *IEEE Trans. Ind. Appl.*, vol. 40, no. 4, pp. 1066–1075, Jul. 2004.

[52] F. Giulii Capponi, G. De Donato, and F. Caricchi, "Recent advances in axial-flux permanent-magnet machine technology," *IEEE Trans. Ind. Appl.*, vol. 48, no. 6, pp. 2190–2205, Nov. 2012.

[53] A. Hemeida, M. Taha, A. A.-E. Abdallh, H. Vansompel, L. Dupre, and P. Sergeant, "Applicability of fractional slot axial flux permanent magnet synchronous machines in the field weakening region," *IEEE Trans. Energy Convers.*, vol. 32, no. 1, pp. 111–121, Mar. 2017.

[54] B. Zhang, S. Andreas, and M. Doppelbauer, "Development of a novel yokeless and segmented armature axial flux machine based on soft magnetic powder composites," in *Proc. World PM Congr. Exhib.*, 2016, vol. 63, no. 4, pp. 2062–2071.

[55] S. Jamali Arand and M. Ardebili, "Multi-objective design and prototyping of a low cogging torque axial-flux PM generator with segmented stator for small-scale direct-drive wind turbines," *IET Electr. Power Appl.*, vol. 10, no. 9, pp. 889–899, Nov. 2016.

[56] S. Y. Gwak, "Characteristic analysis and design of multi-layer buried permanent magnet motor for vehicle traction," Ph.D. dissertation, Dept. Elect. Eng., Seoul Nat. Univ., Seoul, South Korea, 2008.

[57] S. Skoog and A. Acquaviva, "Pole-slot selection considerations for double layer three-phase tooth-coil wound electrical machines," in *Proc. XIII Int. Conf. Electr. Mach. (ICEM)*, Sep. 2018, pp. 934–940.

[58] F. Meier and J. Soulard, "PMSMs with non-overlapping concentrated windings: Design guidelines and model references," *Ecol. Vehicles Renew. Energies*, vol. 09, pp. 26–29, Sep. 2009.

[59] M. Aydin, S. Huang, and T. A. Lipo, "Design, analysis, and control of a hybrid field-controlled axial-flux permanent-magnet motor," *IEEE Trans. Ind. Electron.*, vol. 57, no. 1, pp. 78–87, Jan. 2010.

[60] C. A. Rabbath and D. Corriveau, "A comparison of piecewise cubic Hermite interpolating polynomials, cubic splines and piecewise linear functions for the approximation of projectile aerodynamics," *Defence Technol.*, vol. 15, no. 5, pp. 741–757, Oct. 2019.

[61] A. Hemeida, B. Hannon, H. Vansompel, and P. Sergeant, "Comparison of three analytical methods for the precise calculation of cogging torque and torque ripple in axial flux PM machines," *Math. Problems Eng.*, vol. 2016, Oct. 2016, Art. no. 2171547.

[62] M. Aydin, Z. Q. Zhu, T. A. Lipo, and D. Howe, "Minimization of cogging torque in axial-flux permanent-magnet machines: Design concepts," *IEEE Trans. Magn.*, vol. 43, no. 9, pp. 3614–3622, Sep. 2007.
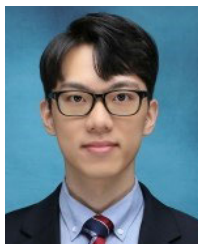
BYUNG-OH TAK received the B.S. degree in electrical and electronics engineering from Chung-Ang University, Seoul, South Korea, in 2019, where he is currently pursuing the M.S. degree as a Graduate Research Assistant. His research interests include the analysis and optimal design of electrical machines and applications of electromagnetic smart materials.

JONGSUK RO (Member, IEEE) received the B.S. degree in mechanical engineering from Han-Yang University, Seoul, South Korea, in 2001, and the Ph.D. degree in electrical engineering from Seoul National University (SNU), Seoul, in 2008.

He is currently an Associate Professor with the School of Electrical and Electronics Engineering, Chung-Ang University, Seoul, South Korea. In 2014, he was with the University of BATH, Bath, U.K., as an Academic Visitor. From 2013 to 2016, he worked with the Brain Korea 21 Plus, SNU, as a BK Assistant Professor. He conducted research at the Electrical Energy Conversion System Research Division of the Korea Electrical Engineering and Science Research Institute as a Researcher, in 2013. From 2012 to 2013, he was with the Brain Korea 21 Information Technology of SNU, as a Postdoctoral Fellow. He conducted research at the Research and Development Center, Samsung Electronics, as a Senior Engineer, from 2008 to 2012. His research interests include the analysis and optimal design of next-generation electrical machines using smart materials such as electromagnet, piezoelectric, and magnetic shape memory alloy.

• • •